Research Article Vol. 15, No. 12 / 1 Dec 2025 / Optical Materials Express 3129
Optical Materials EXPRESS

Design and experimental validation of a high-efficiency multi-zone metasurface waveguide in-coupler

PEI XIONG,[1] JEREMY GOODSELL,[1] DANIEL NIKOLOV,[1,2] JANNICK P. ROLLAND,[1,2] AND NICK A. VAMIVAKAS[1,2,3,4,5,*]

[1]Institute of Optics, University of Rochester, 480 Intercampus Dr, Rochester, NY 14627, USA
[2]Center for Extended Reality, University of Rochester, Rochester, NY 14627, USA
[3]Department of Physics, University of Rochester, 500 Wilson Blvd, Rochester, NY 14627, USA
[4]Materials Science, University of Rochester, Rochester, NY 14627, USA
[5]Center for Coherence and Quantum Optics, University of Rochester, Rochester, NY 14627, USA
*nick.vamivakas@rochester.edu

Abstract: Augmented reality waveguide displays often suffer from low efficiency, inherently caused by losses from multiple interactions of incoming light with the in-coupler. These losses impose a fundamental limitation on system brightness and lead to field-dependent losses (i.e., losses that depend on the angle of incidence on the in-coupler). While previous theoretical work established the field-dependent in-coupling efficiency limit and introduced a multi-zone in-coupler architecture, that analysis was based on idealized assumptions. We present the first experimental realization, design optimization, and rigorous validation of a three-zone metasurface in-coupler that approaches the theoretical efficiency limit for a given waveguide geometry under realistic operating conditions. Each metasurface zone is individually optimized using rigorous coupled-wave analysis, guided by a custom feedback loop that incorporates realistic diffraction efficiency targets based on simulated metasurface performance. This optimization process was adapted to include real-world factors like material loss and non-ideal coupling efficiency sums. The metasurfaces are fabricated using atomic layer deposition and are experimentally characterized via diffraction and reflection measurements. The simulated field-dependent in-coupling efficiency across the horizontal field agrees well with the measured efficiency, confirming the validity of our multi-zone optimization strategy for practical device engineering. This study exemplifies the practical feasibility of metasurface-based in-couplers for waveguide displays and establishes a critical, experimentally proven pathway toward high-efficiency augmented reality displays, directly addressing the input coupling efficiency bottleneck.

1. Introduction

Augmented reality (AR) head-worn displays, first demonstrated by Ivan Sutherland in 1965 and revived in the 90s to this day, are a category of technologies that superimpose computer-generated content onto the user's field of view (FOV) [1–8]. These systems have been applied across a wide range of domains, including education, entertainment, engineering, and medicine [9]. A key element of head-worn AR devices is the optical combiner, which merges virtual images from the display engine with the real world, enabling users to perceive both at the same time [10,11]. Various designs for optical combiners have been explored, such as freeform mirrors and prisms [12–15], birdbath architectures [16], retinal scanning displays [17,18], and waveguide-based combiners [19–29]. Among these options, currently, waveguide combiners are a favored solution due to their compact form factor and mature manufacturing methods. Critically, waveguide displays also provide a large eyebox, which is crucial for ensuring visual comfort during prolonged usage.

#576634 https://doi.org/10.1364/OME.576634
Journal © 2025 Received 26 Aug 2025; revised 17 Oct 2025; accepted 19 Oct 2025; published 11 Nov 2025

Optical Materials EXPRESS

Waveguide combiners use exit pupil expansion to enlarge the eyebox size while preserving the FOV. Exit pupil expansion leverages total internal reflection (TIR) to confine light within the waveguide and replicate the pupil through controlled partial out-coupling. Figure 1 shows the L-shape waveguide design, which uses an expander and an out-coupler to achieve pupil expansion in two orthogonal directions. As depicted in Fig. 1, the in-coupler directs incident light from the display engine into the waveguide by adjusting the angles of the rays to satisfy the TIR condition. Subsequently, the expander modifies the directions of the rays to propagate light towards the out-coupler. The light reflection and transmission at each interaction with the expander are carefully managed to allow each ray to be replicated along the propagation direction, as shown in Fig. 1. Upon reaching the out-coupler, the directions of rays are altered to break the TIR condition, allowing light to exit the waveguide and get to the eye. The out-coupling efficiency at various regions of the out-coupler is similarly adjusted to provide a replication in the direction perpendicular to the expander before exiting the waveguide. This mechanism effectively replicates each incident ray into multiple out-coupled rays, thereby expanding the exit pupil dimensions in 2D.

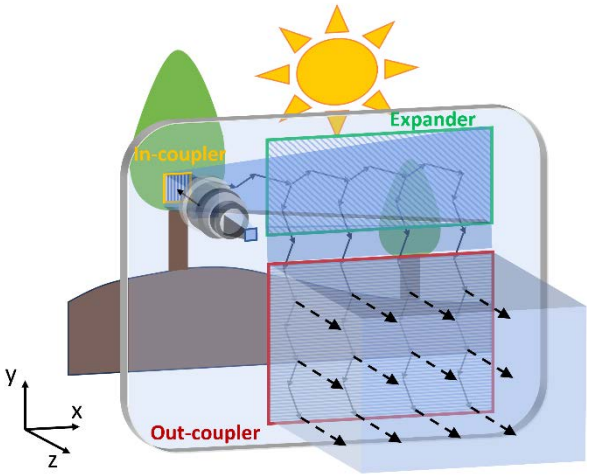

Fig. 1. Working principle of AR waveguide display.

The ray angle adjustments can be achieved via diffraction or reflection, leading to two main types of waveguide combiners, diffractive and reflective waveguides. Diffractive waveguides usually use surface-relief gratings or metasurfaces as couplers. Metasurfaces, composed of subwavelength structures, enable precise control over light's phase, amplitude, and direction [30–36]. Their compactness and design flexibility make them well-suited for integration into waveguide systems, offering an alternative to conventional gratings [24,37–41]. Reflective or geometrical waveguides generally use embedded partial mirrors or prisms, leading to thicker architecture. Each of these different coupling methods presents trade-offs in terms of efficiency, spectral bandwidth, and fabrication complexity.

Regardless of the type of waveguide combiner, the pupil expansion process leads to a decrease in the brightness of out-coupled rays due to the principles of energy conservation. This is indeed a major trade-off for waveguide technology. Therefore, optimizing the coupler design is essential to ensure sufficient out-coupling efficiency to deliver a bright and uniform visual output.

Noted that the in-coupling efficiency fundamentally limits the overall brightness of the system, as any light lost at the in-coupler cannot be recovered later. However, achieving high in-coupling efficiency is challenging due to internal losses caused by the multiple interactions of the incoming light with the in-coupler [24,27,29,42]. As shown in Fig. 2(a), due to the thin profile of the

Optical Materials EXPRESS

waveguide (e.g., 0.5 mm thickness) and the relatively large size of the in-coupler (e.g., 3 mm square), light that initially enters the waveguide can undergo TIR and re-encounter the in-coupler [24]. During these secondary interactions, a portion of the light may couple out of the waveguide in an unintended direction, causing efficiency loss and potential stray light. This problem exists for both diffractive and reflective waveguide architectures [25]. To maximize in-coupling efficiency, the sum of the first-order diffraction efficiency for the incident light (Fig. 2(b)) and the zeroth-order reflection efficiency for the internally trapped light (Fig. 2(c)) must be high to ensure maximum light is retained within the system for subsequent coupling rounds. Due to the principles of light reversibility and energy conservation, this sum cannot exceed 100% [24,27,42].

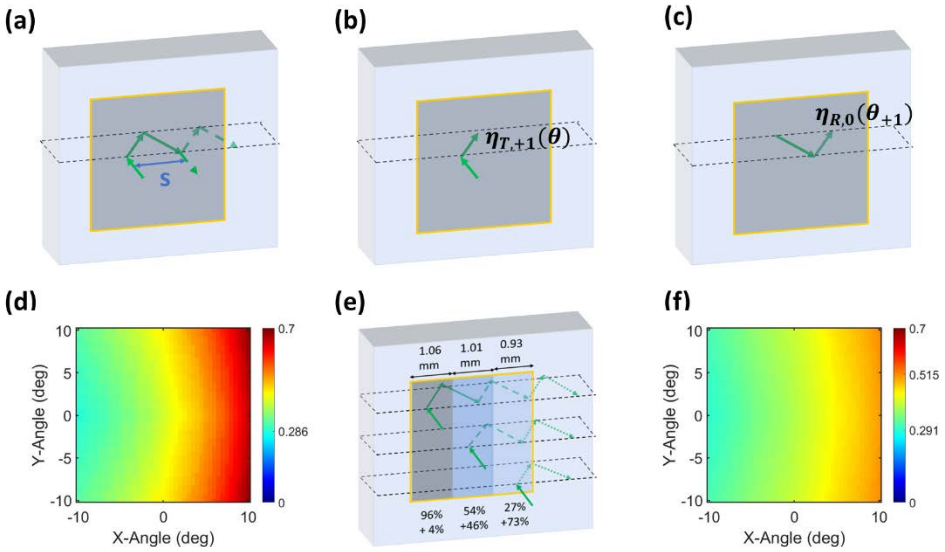

Fig. 2. (a) Multiple interactions problem: a ray from the display engine interacts with the in-coupler (dark grey square), diffracts into the first diffraction order, reflects from the back surface, and interacts with the in-coupler again, part of the light is diffracted and exits out (dashed green arrow outside of the waveguide), the rest of the light is reflected and keeps propagating inside the waveguide (two dashed green arrows inside the waveguide); (b) & (c): Two interactions that affect the final in-coupling efficiency: (b) the diffraction of the incident light into first-order with an efficiency $\eta_{T,+1}(\theta)$, where T means the transmission side, +1 is the order number, and θ is the incident angle; (c) the reflection of the trapped light with an efficiency the $\eta_{R,0}(\theta_{+1})$, where the θ_{+1} means the incident angle for this interaction is the first-order diffraction angle from the interaction in (b); (d) Theoretical coupling efficiency map; (e) Three-zone in-coupler configuration: the values on top of each zone are the sizes of each zone, and the values below each zone are the efficiencies required for each zone, the top rows are the first-order diffraction efficiency required values, and the bottom rows are the zeroth-order reflection efficiencies. (f) The coupling efficiency map calculated for the three-zone in-coupler in (e). Panels (d), (e), and (f) are adapted from the theoretical framework and optimization results presented in Ref. [27].

The multiple interaction problem can be mitigated by either reducing the size of the in-coupler or exit pupil, or by increasing the thickness of the waveguide to increase the separation between TIR paths. However, decreasing the in-coupler or pupil size limits the best achievable image resolution, as the pupil dimension determines the cutoff frequency of the diffraction-limited modulation transfer function (MTF) [43]. Increasing the waveguide thickness compromises the compactness of the display and contributes to additional weight, which is undesirable for wearable

Optical Materials EXPRESS

applications. Moreover, the separation between TIR paths corresponds to the spatial separation between replicated pupils. To preserve high image quality, gaps between these replicated pupils must be minimized, which requires that the maximum TIR separation be at least equal to the pupil size, or the in-coupler size if the two are co-planar. Under this constraint, any field with a smaller TIR separation will inevitably undergo multiple interactions with the in-coupler. Therefore, this problem cannot be entirely avoided through pupil size or waveguide thickness adjustment [29].

Considering the inevitability of this issue, for a given waveguide geometry and in-coupler size and shape, we can derive a fundamental limit on in-coupling efficiency, under the assumption that the combined efficiency of the two interactions shown in Fig. 2(b) & 2(c) totals 100% [24]. The minimum field efficiency (MFE), defined as the minimum in-coupling efficiency for the fields within the FOV, is used as a critical performance metric, as it establishes the upper limit of brightness required for achieving a uniform output. This is because areas exhibiting low efficiency cannot be digitally brightened, while high-efficiency regions can be attenuated. Under typical design parameters (N-BK7 waveguide, 0.5 mm thickness, 3 mm x 3 mm pupil size, 532 nm wavelength, and 20° x 20° FOV), and the case that the pupil and the input coupler are equally sized and co-planar, the theoretical maximum MFE has been calculated to be 29%, as illustrated in Fig. 2(d).

The losses induced by the multiple interactions with the in-coupler result in a field-dependent non-uniform irradiance in the pupil plane that manifests in a reduction in image quality. In prior work, it was shown that splitting the in-coupler into multiple zones with a set of target efficiencies for each zone can maintain the theoretical maximum MFE, while allowing for a diffraction-limited image quality for all fields, specifically a diffraction-limited MTF at 30 cycles per degree (a frequency corresponding to excellent human visual acuity or 20/20 vision) [27]. For the multiple zones configuration optimization, the first-order diffraction efficiency for each zone, as well as the corresponding zone width, are the optimization variables, while the zeroth-order reflection efficiency for each zone can then be determined by the perfect 100% efficiency sum assumption. The optimization merit function includes the coupling efficiency and the MTF values at 30 cycles per degree for the worst field (-10°, 0°). Using this optimization method, a three-zone design with a set of target efficiencies (Fig. 2(e)) was demonstrated for the geometry shown in Fig. 2. In the current study, we provide the first experimental validation and practical implementation of the multi-zone in-coupler using metasurfaces for this three-zone configuration. Each zone was realized with a metasurface, achieving an MFE of 25.3%, which approaches the theoretical limit of 29%. The design process was guided by a custom optimization framework that explicitly incorporates realistic efficiency values and accounts for non-ideal efficiency sums and material loss via a feedback loop for iterative refinement. The fabricated metasurfaces were experimentally characterized using two separate setups: one for measuring grating efficiency separately and another for evaluating coupling efficiency. This successful experimental realization successfully bridges the gap between the idealized theory of Ref. [27] and a real-world AR component, proving a critical, high-efficiency solution that directly addresses the AR brightness bottleneck.

2. Metasurface in-coupler optimization

To design the metasurface for each zone, photonic simulations were conducted using the rigorous coupled-wave analysis (RCWA) method in RSoft (Keysight, former Synopsys). Titanium dioxide (TiO_2) was chosen as the meta-atom material because of its high refractive index and low absorption in the visible spectrum, which makes it an ideal choice for waveguide-based optical combiners. Each metasurface design consists of periodic arrays of nano-beams and nano-pillars as illustrated in Fig. 3(a). The grating period is set to 453 nm, which is derived from the system specification that the smallest diffraction angle for the field (-10°, 0°) is just larger than the critical angle of N-BK7. As indicated by the target efficiency distribution in Fig. 2(e), each zone requires two distinct efficiency values that correspond to separate interactions shown in Fig. 2(b) and

Optical Materials EXPRESS

Fig. 2(c). To simplify the metasurface optimization, only the XFOV is scanned to obtain the diffraction efficiencies since these efficiencies are nearly constant along the vertical directions. To further reduce computational complexity, equivalent interactions that share the same incident direction are used in the simulation, based on the principle of light reversibility, as described in Supplement S1. The light source is TE-polarized green light with a wavelength of 532 nm. The source is located within the glass substrate, and the incident angle varies from 41.5° to 62.5°, corresponding to the range of first-order diffraction angles for incident angles spanning from -10° to 10°, according to the grating equation in transmission given as:

$$n_d \sin(\theta_d) = n_i \sin(\theta_i) + \frac{m\lambda}{d},$$

where n_d and n_i are the refractive indices of the medium on the diffraction and incident sides, respectively. θ_d and θ_i are the diffraction and incident angles, m is the diffraction order, λ is the wavelength, and d is the grating period.

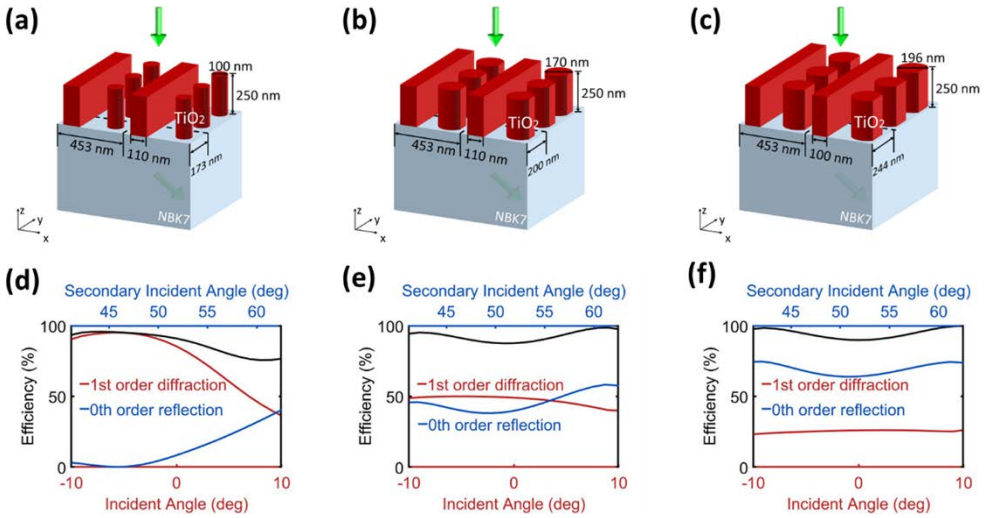

Fig. 3. Metasurface designs for a three-zone in-coupler configuration: (a)-(c) metasurface geometries for zones 1-3, respectively; (d)-(f) efficiency curves for metasurface designs (a)-(c), where the red curves represent the first-order diffraction efficiency as a function of incident angle from -10° to 10°, and the blue curves represent the zeroth-order reflection efficiency as a function of secondary incident angle from 41.2° to 62.5°, and the black curves are the sum of the two efficiencies.

The design variables consist of the width of the nano-beam, the diameter and thickness of the nano-pillar, the separation between the nano-beam and nano-pillar, and the unit cell size along the y-direction. For each simulation, the outputs include the first-order diffraction efficiency and the zeroth-order reflection efficiency. The merit function is defined as the deviation between these simulated efficiencies and the respective target values. Optimization is performed using the Multi-Variable Optimization and Scanning Tool (MOST) in RSoft to minimize this deviation and achieve the desired performance.

The target efficiencies shown in Fig. 2(e) assume the ideal scenario where the sum of the two interaction efficiencies equals 100%. However, absorption and additional diffraction orders exist in practical applications for real gratings, resulting in a combined efficiency of less than 100% (see Supplement S1). These actual values must be updated within the optimizer to re-optimize the efficiency distribution for the three-zone architecture to get a more realistic target for the metasurface optimization. The complete optimization workflow is detailed in Supplement S2.

Optical Materials EXPRESS

Following this workflow, the optimized metasurface geometries for each zone are presented in Fig. 3(a)–3(c). All three designs share the same thickness, which is a constraint imposed to accommodate fabrication. In zones 2 and 3, the nano-pillars display partial circular shapes as the pillar dimensions were allowed to exceed unit cell boundaries during optimization.

The first-order diffraction efficiencies as functions of the horizontal field of view (XFOV) are shown in Fig. 3(d)–3(f) for the three metasurface designs. In Fig. 3(d), the diffraction efficiency of zone 1 is non-uniform across the XFOV, showing a high value at the left end and a gradual decrease toward the right end. This trend is similar to the performance observed in a single-zone metasurface in-coupler discussed in our previous study [24]. The optimization merit function is adjusted to balance the efficiencies at both ends of the XFOV, attaining a high efficiency at the left end (-10°, 0°) and preventing the efficiency at the other end from dropping too much due to the limited angular bandwidth. In contrast, zones 2 and 3 demonstrate much flatter efficiency curves, although they are optimized only for the −10° field angle. This suggests that the designs for zones 2 and 3 inherently provide broader angular bandwidths than zone 1. These results also emphasize a trade-off between peak efficiency and angular bandwidth in this class of metasurfaces.

3. Metasurface evaluation using a ray tracing model

A simplified AR waveguide display is modeled in non-sequential ray-tracing software (LightTools from from Keysight, former Synopsys) to evaluate the performance of the designed metasurface in-coupler. As shown in Fig. 4(a), the left portion of the system includes the display engine, which consists of a light source, two ideal lenses serving as a collimator, and a linear polarizer. The polarizer is used to ensure that the incident light is TE-polarized, as the metasurfaces are optimized for this polarization state. The metasurface in-coupler zones are defined by their bidirectional scattering distribution function (BSDF). The out-coupler is modeled as an ideal grating with 100% efficiency to extract the trapped light from the waveguide. An additional perfect lens is positioned to focus the collimated light from the out-coupler onto the detector plane for final assessment.

The designed display engine over-illuminates the in-coupler area due to the circular shape of the exit pupil, while the in-coupler has a square geometry. To address this mismatch, a spatial filter is used to collect the portion of light that enters the square in-coupler region. A more efficient solution would be to reshape the circular exit pupil into a square geometry at the in-coupler using freeform optics. [15,44]. Based on the measured light distribution at the detector, the coupling efficiency is calculated as the ratio of the irradiance at the detector to the irradiance from the input source after filtering. As shown in Fig. 4(b), the MFE for the three-zone metasurface in-coupler is 25.3%, occurring at an XFOV of –10°. The efficiency drop observed at positive incident angles for zone 1 [Fig. 3(d)] does not lower the MFE. Instead, it contributes to a more uniform coupling efficiency distribution across the entire field of view. To better align with the measurement method mentioned below for coupling efficiency measurement, the prism-based out-coupling is also simulated, as shown in Fig. 4(c). A detector is positioned right after the prism to capture the out-coupled light. An array of point sources is used as the light source, and they are activated individually to sample the XFOV. The measured coupling efficiency dots are shown in Fig. 4(d), and they match well with the XFOV cross section of Fig. 4(b).

4. Metasurface fabrication

The aspect ratio of the designed metasurfaces, one for each zone, defined as the ratio of the structure's height to its lateral size in the x-y plane, reaches up to 2.5 for the nanobeams in zone 3. For this aspect ratio, both etching and atomic layer deposition (ALD) methods are suitable for fabrication. In this study, the ALD method is selected due to its ability to produce TiO_2 films with a higher refractive index compared to the sputtered TiO_2 used in etching processes.

Optical Materials EXPRESS

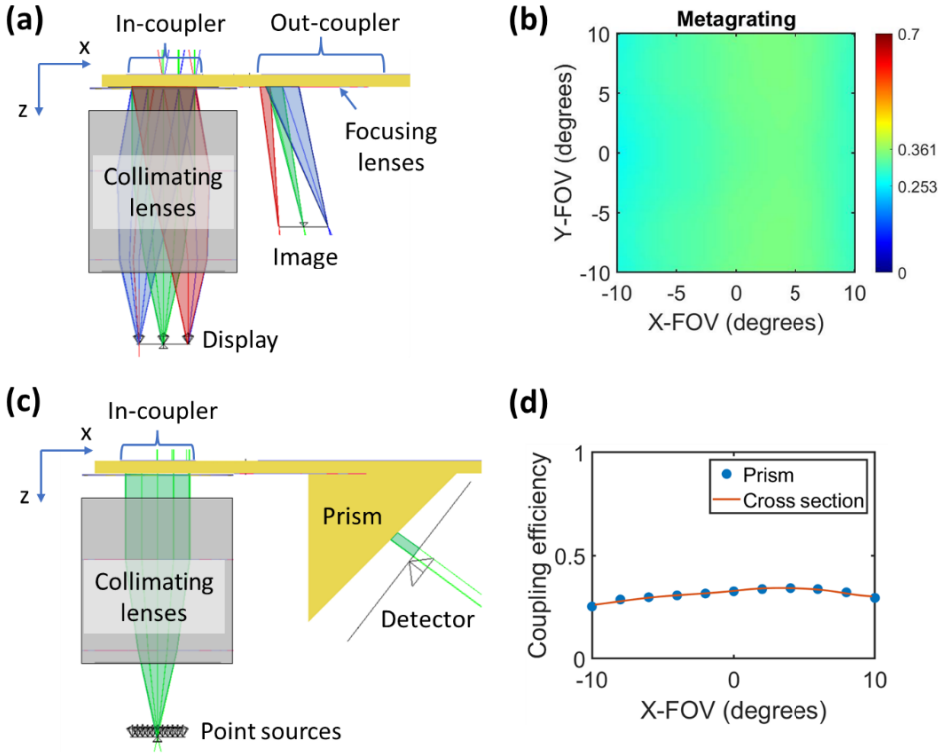

Fig. 4. LightTools evaluation of the three-zone metasurfaces in-coupler: (a) geometry modeled in LightTools for evaluating coupling efficiency; (b) simulated coupling efficiency map using the metasurfaces as the three-zone in-coupler, exemplifying uniformity; (c) geometry modeled using a prism as out-coupler; (d) simulated coupling efficiency using the prism compared with the cross section along XFOV in Fig. 4(b).

Figure 5(a) outlines the fabrication steps using the ALD method. First, a diluted PMMA (MicroChem), which is a positive electron beam lithography resist, is spin-coated onto an N-BK7 substrate at 1800rpm for 60 seconds. This step produces a 300 nm-thick resist layer, which is thicker than the height of the TiO_2 structures to account for material loss during descumming and over-etching. The resist is then baked at 170 °C for 15 minutes. To reduce the charging effect during electron beam exposure, DisCharge H2Ox2 (DisChem) is spin-coated at 2000rpm for 60 seconds. Pattern exposure is then carried out using a 100 kV JEOL 9500 electron beam lithography system. After exposure, the sample is rinsed in deionized water for 30 seconds to remove the discharge layer, then developed in a 1:3 MIBK/IPA solution for 45 seconds, rinsed in IPA for 30 seconds, and dried with nitrogen gas. A 20-second Argon plasma descum step follows to remove residual resist. In the next step, a TiO_2 layer is deposited using a Cambridge Savannah 200 ALD system with TDMAT and water as precursors. Each cycle includes a 0.1-second TDMAT pulse, a 25-second delay, a 0.015-second water pulse, and another 25-second delay. The chamber temperature is kept at 85 °C, and the TDMAT precursor is held at 70 °C. This process results in a deposition rate of approximately 0.065 nm per cycle. Next, reactive ion etching is performed using an inductively coupled plasma (ICP) system (PlasmaTherm) with $BCl_3/Cl_2/Ar$ gases (30/2/7 sccm), at an RF power of 50 W and an ICP power of 800 W. The etching rate is approximately 66 nm/min. Finally, oxygen plasma is used to remove degraded resist, and the remaining resist is dissolved in acetone overnight.

Optical Materials EXPRESS

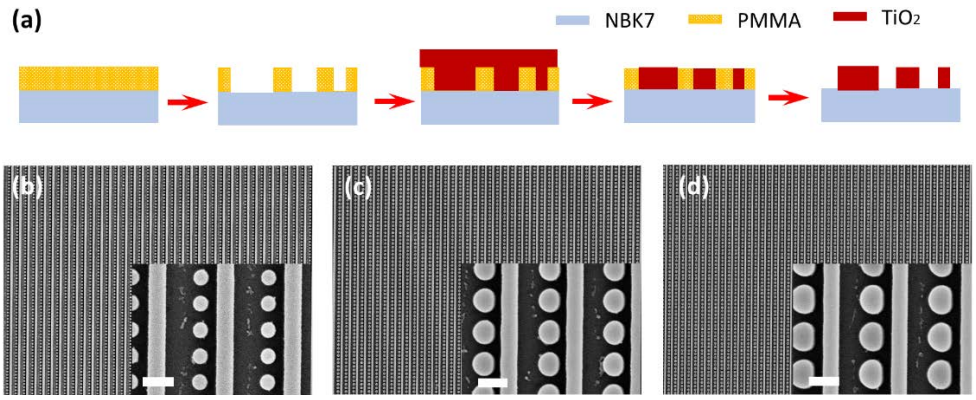

Fig. 5. Metasurface fabrication: (a) fabrication workflow of the ALD method; (b)-(d) SEM images showing the top views of the fabricated metasurface zones 1-3, respectively. The insets provide a zoomed-in view of the metasurfaces, with a scale bar of 200 nm.

Figures 5(b)–5(d) show top-view scanning electron microscope (SEM) images of the fabricated metasurfaces for different zones. The insets provide zoomed-in views. The fabricated meta-atom shapes closely match the simulation results, and the variations are within ±20 nm, as shown in Table 1. However, as shown in the insets of Figs. 5(c) and 5(d), the sharp corners of the partially circular structures in zones 2 and 3 appear slightly rounded**.**

Table 1. Comparison between designed and measured geometries for zone 1-3 metasurfaces

	Zone 1		Zone 2			Zone 3		
	Bar width	Pillar diameter	Bar width	Pillar diameter	Pillar width	Bar width	Pillar diameter	Pillar width
Designed value (nm)	110	100	110	170	156.5	100	196	160.5
Measured value (nm)	110.5	97.98	110.3	156.9	136.4	100.1	190.2	149.5

5. Metasurface measurements

5.1. Diffraction and reflection efficiencies measurement

The first-order diffraction efficiency of the fabricated metasurface in-coupler was measured using the experimental setup illustrated in Fig. 6(a). A green laser is first coupled into a single-mode fiber, with the output end connected to a fiber collimator (Thorlabs CFS18-532-FC), producing a collimated beam with a diameter of approximately 3.5 mm. To measure the efficiency of individual metasurfaces, three metasurfaces are fabricated at separate locations for each zone, each with a size of 800 µm square. A pinhole with a diameter of 800 µm is placed below the collimator to ensure that the incident beam size is smaller than that of the metasurfaces, and a linear polarizer is positioned to generate TE-polarized incident light. The collimator, pinhole, and polarizer are mounted together on an arm of the rotational stage to allow control over the angle of incidence.

The sample is mounted on a custom-built stage that includes three-axis translation (x, y, z) and a tip-tilt mechanism, providing the full range of motion required for precise alignment. Diffraction efficiency measurements are performed over incidence angles ranging from -10° to 10° with a step of 2°, corresponding to the system's horizontal field of view (XFOV). A

Optical Materials EXPRESS

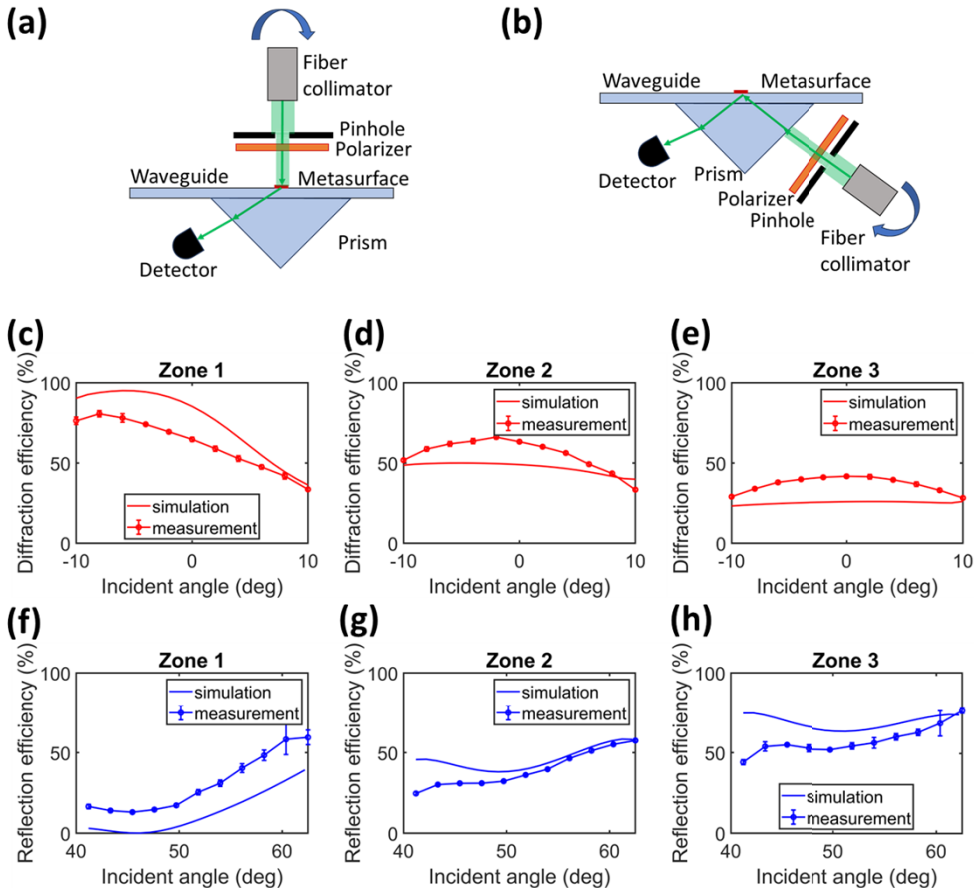

Fig. 6. Metasurface interaction efficiency measurements: (a) experimental setup for first-order diffraction efficiency measurement; (b) experimental setup for zeroth-order reflection efficiency measurement; (c)-(e) measured first-order diffraction efficiency for zones 1-3, respectively; (f)-(h) measured zeroth-order reflection efficiency for zones 1-3, respectively.

N-BK7 prism is used to extract the diffracted light and is attached to the waveguide using a BK-7 matching liquid (Cargille). A photodiode is positioned after the prism to collect the power of the diffracted light. The photodiode also measures the incident power just before the metasurface to determine the diffraction efficiency. The zeroth-order reflection efficiency is measured similarly, as shown in Fig. 6(b), by placing the illumination arm on the opposite side of the waveguide. For this reflection efficiency measurement, the incident angle is adjusted to vary from 39.22° to 72.17° in air, which corresponds to the first-order diffraction angle range of 42.5° to 62.5° in N-BK7 glass.

The measurements for the first-order diffraction efficiencies are shown in Fig. 6(c)–6(e). For all three zones, the measured efficiencies display a similar trend as a function of incident angle compared to the simulation results, with slight offsets in the efficiency values. For instance, there is an efficiency drop on the left side of the XFOV for the zone 1 metasurface compared to the simulation result. Additionally, there is an efficiency increase in the middle XFOV for the zone 2 and 3 metasurfaces. The measurements for the zeroth-order reflection efficiencies are shown in Fig. 6(f)–6(h). The measured efficiencies also exhibit the same trend as a function of incident angle when compared to the simulation results. For the zone 1 metasurface, the

Optical Materials EXPRESS

measured reflection efficiencies are consistently greater than the simulated reflection efficiencies across the incident angle range. In contrast, for zones 2 and 3, the measured reflection efficiency is lower than the simulated reflection efficiency at the left end of the FOV but converges to match it as the incident angle increases.

5.2. Coupling efficiency measurement

The coupling efficiency of the fabricated metasurface three-zone in-coupler was measured using a similar experimental setup compared to the measurement of the above efficiencies, as illustrated in Fig. 7(a). The fiber collimator (Thorlabs F810FC-543) is different, producing a larger beam diameter of approximately 6.4 mm. The pinhole has been replaced with a custom square aperture with a size of 3 mm by 3 mm. The in-coupler is aligned to the center of the rotary arm, so it can stay still while the arm is rotating to change the angle of incidence. The N-BK7 prism is now positioned on the side of the in-coupler and is used to extract the light guided within the waveguide.

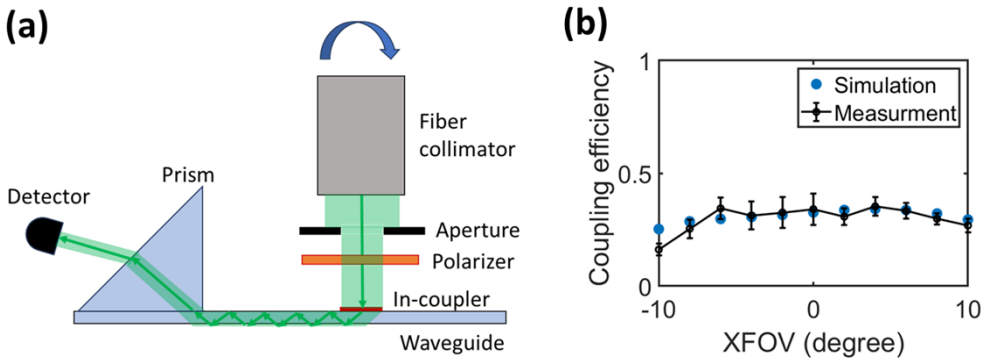

Fig. 7. Measurement of coupling efficiency for the metasurface in-coupler: (a) experimental setup for measuring coupling efficiency; (b) coupling efficiency measured along the XFOV.

The measured coupling efficiency along the XFOV for the fabricated metasurface in-coupler is shown in Fig. 4(b). The simulation result using the out-coupling prism is represented as the dots in the plot, while the measured data is indicated by the error bars. This data aligns closely with the simulation results, except for the field (-10°, 0°). The simulated coupling efficiency for the (-10°, 0°) field is 25.3%, whereas the measured coupling efficiency is approximately 17%. This drop in efficiency can be predicted by the measured efficiency results in the section above. For zone 1, the measured first-order diffraction efficiency is lower than the simulated result at the field (-10°, 0°), while the zeroth-order reflection efficiency is higher, and the sum of the two efficiencies is close to 1. In zones 2 and 3, although the measured first-order diffraction efficiency is the same as or slightly higher than the simulated results, the zeroth-order reflection efficiency is much lower, causing a decrease in the coupling efficiency for that field. When these measured efficiency data are used to calculate the coupling efficiency, using the same method as the theoretical coupling efficiency limit [24], the result is 17.7% for field (-10°, 0°), which is close to the measured result. The maximum offset between the measured reflection efficiency and the simulated reflection efficiency at the field (-10°, 0°) for both zones 2 and 3 might be due to the alignment error of the measurement, since the simulated reflection efficiency drops quickly when going further to the left of the XFOV. For the coupling efficiency drop at the same field, the alignment error might be one cause, and another reason might be that the diffraction angle for this field is just larger than the critical angle. If there are fabrication errors causing a grating period mismatch, the diffracted light won't be trapped inside the waveguide.

Optical Materials EXPRESS

6. Conclusions

We have demonstrated the design, fabrication, and experimental validation of a three-zone metasurface in-coupler that approaches the theoretical in-coupling efficiency limit for AR waveguide displays. This work successfully translates the idealized multi-zone theory into a practical, realized AR component. Each metasurface zone was independently optimized using RCWA simulations, supported by a custom feedback workflow that incorporates realistic, as-built efficiencies and accounts for non-ideal efficiency sums and material loss. The metasurfaces were fabricated using ALD and experimentally characterized, with field-dependent coupling efficiency measurements showing strong agreement with simulation across most of the field of view. The average measured efficiency is 30%, closely matching the simulated average of 31%, confirming consistency across the central field. Minor discrepancies were observed at the edge of the field (-10^o, 0^o), where the measured coupling efficiency is 17%, compared to a simulated efficiency of 25%. We interpret the reasons as fabrication imperfections and angular sensitivity. Overall, the results validate the metasurface designs and, more importantly, confirm the viability of the multi-zone approach under realistic operating conditions. This successful experimental demonstration establishes a practical and scalable pathway for implementing high-efficiency metasurface in-couplers in compact AR waveguide displays, directly addressing the major brightness and power-efficiency bottleneck in next-generation AR systems.

Funding. National Science Foundation (NNCI-2025233, DGE-1922591).

Acknowledgments. This work was performed in part at the Cornell NanoScale Facility, a member of the National Nanotechnology Coordinated Infrastructure (NNCI), which is supported by the National Science Foundation (Grant NNCI-2025233). We also thank the National Science Foundation NRT program (Grant DGE-1922591) for supporting Jeremy Goodsell. We thank Optical Solutions Group from Keysight (former Synopsys) for the student license of RSoft Photonic Device Tools and LightTools, and MathWorks for the student license of MATLAB. We also acknowledge that this research was done in synergy with the Center for Extended Reality (CXR). Finally, we thank the Integrated Nanosystems Center at the University of Rochester for ALD deposition.

Disclosures. The authors declare no conflicts of interest.

Data availability. The paper and the Supplementary Materials present all the data needed to evaluate the conclusions. Additional data related to this paper may be requested from the authors.

Supplemental document. See Supplement 1 for supporting content.

References

1. I. E. Sutherland, "The ultimate display," in *Proceedings of the IFIP Congress*, (New York, 1965), 506–508.
2. J. P. Rolland and H. Fuchs, "Optical versus video see-through head-mounted displays," in *Fundamentals of Wearable Computers and Augmented Reality* (CRC Press, 2001), pp. 129–172.
3. O. Cakmakci and J. Rolland, "Head-worn displays: a review," J. Display Technol. **2**(3), 199–216 (2006).
4. J. P. Rolland, K. P. Thompson, H. Urey, *et al.*, "See-Through Head Worn Display (HWD) Architectures," in *Handbook of Visual Display Technology*, J. Chen, W. Cranton, and M. Fihn, eds. (Springer Berlin Heidelberg, Berlin, Heidelberg, 2012), pp. 2145–2170.
5. B. C. Kress, *Optical Architectures for Augmented-, Virtual-, and Mixed-Reality Headsets* (SPIE Press, 2020).
6. T. Zhan, K. Yin, J. Xiong, *et al.*, "Augmented reality and virtual reality displays: perspectives and challenges," iScience **23**, 101397 (2020).
7. J. Xiong, E.-L. Hsiang, Z. He, *et al.*, "Augmented reality and virtual reality displays: emerging technologies and future perspectives," Light: Sci. Appl. **10**(1), 216 (2021).
8. J. P. Rolland, K. P. Thompson, H. Urey, *et al.*, "See-Through Head-Worn Display (HWD) Architectures," in *Handbook of Visual Display Technology* (Springer, 2025), pp. 1–34.
9. S. C.-Y. Yuen, G. Yaoyuneyong, E. Johnson, *et al.*, "Augmented reality: An overview and five directions for AR in education," Journal of Educational Technology Development and Exchange (JETDE) **4**, 11 (2011).
10. T. Furness, "Helmet-mounted displays and their aerospace applications," in *National Aerospace Electronics Conference*, (1969),
11. J. P. Rolland, "Wide-angle, off-axis, see-through head-mounted display," Opt. Eng. **39**(7), 1760–1767 (2000).
12. O. Cakmakci and J. Rolland, "Design and fabrication of a dual-element off-axis near-eye optical magnifier," Opt. Lett. **32**(11), 1363–1365 (2007).
13. D. Cheng, Y. Wang, H. Hua, *et al.*, "Design of an optical see-through head-mounted display with a low f-number and large field of view using a freeform prism," Appl. Opt. **48**(14), 2655–2668 (2009).

Optical Materials EXPRESS

14. A. Bauer and J. P. Rolland, "Visual space assessment of two all-reflective, freeform, optical see-through head-worn displays," Opt. Express **22**(11), 13155–13163 (2014).
15. J. P. Rolland, M. A. Davies, T. J. Suleski, *et al.*, "Freeform optics for imaging," Optica **8**(2), 161–176 (2021).
16. M. B. Spitzer, N. M. Rensing, R. McClelland, *et al.*, "Eyeglass-based systems for wearable computing," in *Digest of papers. First international symposium on wearable computers*, (IEEE, 1997), 48–51.
17. I. Thomas A. Furness and J. S. Kollin, "VIRTUAL RETINAL DISPLAY," (1995).
18. M. M. Bayer, "Retinal scanning display: a novel HMD approach for army aviation," in *Helmet-and Head-Mounted Displays VII*, (SPIE, 2002), 202–213.
19. M. Xu and H. Hua, "Ultrathin optical combiner with microstructure mirrors in augmented reality," in *Digital Optics for Immersive Displays*, (SPIE, 2018), 257–271.
20. T. Yoshida, K. Tokuyama, Y. Takai, *et al.*, "A plastic holographic waveguide combiner for light-weight and highly-transparent augmented reality glasses," J. Soc. Info. Display **26**(5), 280–286 (2018).
21. B. C. Kress, "Optical waveguide combiners for AR headsets: features and limitations," in *Digital Optical Technologies 2019*, (SPIE, 2019), 75–100.
22. B. C. Kress and I. Chatterjee, "Waveguide combiners for mixed reality headsets: a nanophotonics design perspective," Nanophotonics **10**(1), 41–74 (2020).
23. C. T. Draper and P.-A. Blanche, "Holographic curved waveguide combiner for HUD/AR with 1-D pupil expansion," Opt. Express **30**(2), 2503–2516 (2022).
24. J. Goodsell, D. K. Nikolov, A. Nick. Vamivakas, *et al.*, "Metagrating meets the geometry-based efficiency limit for AR waveguide in-couplers," Opt. Express **31**(3), 4599–4614 (2023).
25. Y. Ding, Q. Yang, Y. Li, *et al.*, "Waveguide-based augmented reality displays: perspectives and challenges," eLight **3**(1), 24 (2023).
26. J. P. Rolland and J. Goodsell, "Waveguide-based augmented reality displays: a highlight," Light: Sci. Appl. **13**(1), 22 (2024).
27. J. Goodsell, A. Nick Vamivakas, J. P. Rolland, *et al.*, "Framework for optimizing AR waveguide in-coupler architectures," Opt. Express **32**(6), 9967–9981 (2024).
28. Z. Zhao, Y.-H. Lee, X. Feng, *et al.*, "Theoretical efficiency limit of diffractive input couplers in augmented reality waveguides," Opt. Express **32**(7), 12340–12357 (2024).
29. Y. Ding, Y. Gu, Q. Yang, *et al.*, "Breaking the in-coupling efficiency limit in waveguide-based AR displays with polarization volume gratings," Light: Sci. Appl. **13**(1), 185 (2024).
30. X. Ni, A. V. Kildishev, V. M. Shalaev, *et al.*, "Metasurface holograms for visible light," Nat. Commun. **4**(1), 2807 (2013).
31. N. Yu and F. Capasso, "Flat optics with designer metasurfaces," Nat. Mater. **13**(2), 139–150 (2014).
32. D. Lin, P. Fan, E. Hasman, *et al.*, "Dielectric gradient metasurface optical elements," Science **345**(6194), 298–302 (2014).
33. G. Zheng, H. Mühlenbernd, M. Kenney, *et al.*, "Metasurface holograms reaching 80% efficiency," Nat. Nanotechnol. **10**(4), 308–312 (2015).
34. H.-T. Chen, A. J. Taylor, N. Yu, *et al.*, "A review of metasurfaces: physics and applications," Rep. Prog. Phys. **79**(7), 076401 (2016).
35. A. Arbabi, E. Arbabi, Y. Horie, *et al.*, "Planar metasurface retroreflector," Nat. Photonics **11**(7), 415–420 (2017).
36. H. H. Hsiao, C. H. Chu, D. P. Tsai, *et al.*, "Fundamentals and applications of metasurfaces," Small Methods **1**(4), 1600064 (2017).
37. M. Gopakumar, G.-Y. Lee, S. Choi, *et al.*, "Full-colour 3D holographic augmented-reality displays with metasurface waveguides," Nature **629**(8013), 791–797 (2024).
38. Z. Tian, X. Zhu, P. A. Surman, *et al.*, "An achromatic metasurface waveguide for augmented reality displays," Light: Sci. Appl. **14**(1), 94 (2025).
39. T. Afra, M. R. Salehi, E. Abiri, *et al.*, "Design of two compact waveguide display systems utilizing metasurface gratings as couplers," Appl. Opt. **60**(28), 8756–8765 (2021).
40. W. Song, X. Liang, Q. Cheng, *et al.*, "Full-Color Waveguide-Type Near-Eye Displays with Huygens' Metasurfaces," Adv. Opt. Mater. **13**(17), 2500096 (2025).
41. P. Genevet, F. Capasso, F. Aieta, *et al.*, "Recent advances in planar optics: from plasmonic to dielectric metasurfaces," Optica **4**(1), 139–152 (2017).
42. C. Nelson, M. Granados-Baez, A. Nishant, *et al.*, "Impact of secondary interactions on in-coupler designs for thin waveguide combiners," Opt. Express **33**(16), 33800–33815 (2025).
43. J. W. Goodman, *Introduction to Fourier Optics*, Fourth ed. (W. H. Freeman, 1969), p. 564.
44. J. C. Miñano, P. Benítez, J. Chaves, *et al.*, "Chapter One - Freeform optics design," in *Progress in Optics*, T. D. Visser, ed. (Elsevier, 2022), pp. 1–124.